Terahertz excitation of exchange mode in a cavity formed by crystal interfaces

C. Reinhoffer,[1] I. Razdolski,[2,3] C. Kadlec,[4] P. Stein,[1] F. Kadlec,[4] S. Germanskiy,[1] A. Stupakiewicz,[2] P. H. M. van Loosdrecht,[1] and E. A. Mashkovich[1]

[1]*Institute of Physics II, University of Cologne, 50937 Cologne, Germany*
[2]*Faculty of Physics, University of Białystok, Ciolkowskiego 1L, 15-245 Bialystok, Poland*
[3]*Photonics Research Centre, Universiti Malaya, 50603 Kuala Lumpur, Malaysia*
[4]*Institute of Physics of the Czech Academy of Sciences, Na Slovance 2, 182 00 Prague 8, Czech Republic*

(Received 15 July 2024; revised 8 March 2025; accepted 8 April 2025; published 13 May 2025)

The interaction of terahertz (THz) radiation with high-frequency spin resonances in complex magnetic materials is central for modern ultrafast magnonics. Here we demonstrate strong variations of the excitation efficiency of the sub-THz exchange magnon in a single crystal gadolinium iron garnet $(Gd, Bi)_3Fe_5O_{12}$. An enhancement of the exchange magnon amplitude is observed when its frequency matches an eigenmode of the cavity created by the sample interfaces. Moreover, this enhancement is accompanied by a fivefold decrease in effective damping of the exchange mode. The THz-exchange magnon interaction in the cavity is analyzed within the developed Landau–Lifshitz–Gilbert formalism for three coupled magnetization sublattices and cavity-enhanced THz field. This work presents an approach for the THz excitation of magnetization dynamics in ferrimagnets and outlines promising pathways for the controlled optimization of light-magnetization coupling in single crystals.

DOI: 10.1103/PhysRevB.111.184412

I. INTRODUCTION

The predominant form of data storage technology today is still ferromagnetic based, which limits operational frequencies to a few GHz [1]. To achieve significantly higher frequencies, i.e., in the THz range, antiferromagnetic magnetic recording and control is the subject of intense investigation nowadays [2–13]. Among media with antiferromagnetic ordering, ferrimagnets are especially appealing as they combine the feasibility of magnetic control with high THz-scale eigenfrequencies. One material class at the center of these investigations has been the rare earth iron garnets [10–12,14]. Iron garnets crystallize in the Ia$\bar{3}$d structure where the iron ions form two sublattices sitting in oxygen octahedral $\vec{M}_a$ and tetrahedral sites $\vec{M}_d$ with a ratio of 10 μ_B : 15 μ_B, while the rare earth ions occupy the interstitial sites [15]. By substituting the main rare earth element [16], and by doping with nonmagnetic ions [17], the magnetic properties of these materials become highly tunable. Due to the strong Fe-Fe exchange interaction, iron garnets typically are treated as ferrimagnets characterized by two sublattices: gadolinium $\vec{M}_{Gd} = \vec{M}_c$ and joint iron $\vec{M}_{Fe} = \vec{M}_d + \vec{M}_a$, respectively. The strength of the exchange interaction between these sublattices can be directly probed by measuring the corresponding magnetic exchange mode [18]. The frequency of this resonance is highly sensitive to temperature, especially in the vicinity of the magnetic compensation point, where $|\vec{M}_{Fe}| = |\vec{M}_{Gd}|$. Furthermore, substitution of Gd with Bi enhances the magneto-optical response, enabling ultrafast magneto-optical spectroscopy [19,20]. The exchange mode can be excited either resonantly [21] or via optomagnetic effects [10].

There are several approaches to increase the coupling strength between photons and magnons: Some are based on energy concentration using cavities [22–24], while others exploit multiple terahertz pulses as a stimulus to coherently control the magnon response [25,26]. In this paper, we combine the concepts of cavity engineering with multiple THz pulse excitation to demonstrate the vast tuning possibilities of the coupling strength between light and magnetization at THz frequencies. Specifically, we analyze the practically important case where the cavity is created by the two interfaces of a plane-parallel micron-scale plate made of the ferrimagnet itself. The tunability of the exchange mode frequency through temperature control allows us to couple it with multiple cavity modes in a controllable way. By performing THz-pump optical-probe experiments, we monitor the amplitude and the frequency of the exchange mode to reveal the corresponding magnon-photon coupling strength at various temperatures. The enhancement of the mode amplitude is readily observable when the frequency of the magnon mode is resonant with an eigenmode of the cavity, while a reduction of the effective damping is observed across the full temperature range between 80 and 130 K. Numerical simulation based on Landau–Lifschitz–Gilbert equations in a two-sublattice system in a cavity show good agreement with the experimental findings. Overall, this work touches on a previously unexplored realm of THz cavity spin dynamics and provides a systematic understanding of the dynamical magnetic response of a ferrimagnetic cavity.

II. MATERIALS AND METHODS

A 200 μm thick single crystal of $(Gd, Bi)_3Fe_5O_{12}$ (GdBIG) oriented along the (111) direction was grown using liquid phase epitaxy and polished to the prescribed thickness [10]. The sample was mounted in a continuous flow cryostat and cooled using liquid nitrogen with a dc magnetic field applied in the sample plane. Broadband THz pulses were generated using the tilted-pulse-front optical rectification technique in a

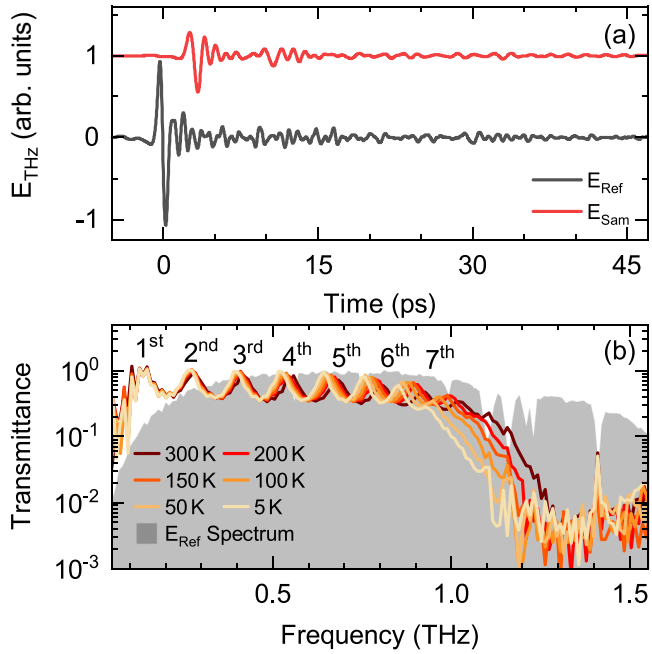

FIG. 1. Static characterization of GdBIG. (a) THz electric field transmitted through the sample E_{Sam} and an empty sample holder E_{Ref} at room temperature, offset for better visibility. (b) Transmission spectrum of GdBIG at different temperatures. The reference spectrum is shown as a gray background, where the sharp absorption lines result from the water vapor absorption. The cavity modes are numbered according to their order.

$LiNbO_3$ crystal [27]. For that optical pulses from a Ti:sapphire amplifier with 6 mJ per pulse, 1 kHz repetition rate, and a center wavelength of 800 nm were used. Part of this beam was split off to be used as a low-intensity probe pulse. Two types of THz spectroscopy experiments were conducted: THz time-domain (TDS) spectroscopy and THz-pump optical-probe (TPOP). In the TDS setup, the THz beam was focused onto the sample using parabolic mirrors. After passing through the GdBIG sample, the beam was collected, and the THz electric field was measured using electro-optic sampling (EOS) with a 1 mm thick ZnTe crystal [28]. In the TPOP experiment, the focused THz beam and an 800 nm probe beam were overlapped within the sample, propagating collinearly through it. After transmitting through the sample, the 800 nm beam passed through a half-wave ($\lambda/2$) plate and a Wollaston prism before being detected using the balanced photodiode technique [28]. This setup enabled the measurement of the THz-induced rotation of the 800 nm beam. Both the THz and optical radiation were at normal incidence. For both experimental configurations, the polarization state and fluence of the THz radiation was controlled using two wire grid polarizers. In TDS the THz electric field strength was reduced below 10 $\frac{kV}{cm}$, whereas for TPOP, THz field strengths up to 700 $\frac{kV}{cm}$ were used.

III. RESULTS

As a first step, the transmission properties of GdBIG were studied by THz TDS spectroscopy at different temperatures. Figure 1(a) shows the THz electric field transmitted through the sample E_{Sam} and the reference THz electric field E_{Ref} at room temperature. The main peak of E_{Sam} is delayed by ∼3.1 ps compared to the reference signal. Furthermore, a second peak at ∼10.7 ps is visible, originating in the back reflection of the THz pulse from the rear interface of GdBIG. For a sample thickness of 200 μm and the time delay observed between E_{Ref} and E_{Sam}, the effective refractive index n, in the <1 THz frequency range, is estimated to be ∼5.6. This rough assumption is in good agreement with precise refractive index measurements shown in Fig. 8.

The amplitude transmission spectra plotted in Fig. 1(b) are calculated as the ratio of the absolute values of the E_{Sam} and E_{Ref} Fourier transform (FT) spectra. A strong periodic modulation of the transmission is observed, which is caused by formation of a THz pulse train due to multiple reflections from both crystal interfaces [29]. The peaks shift to lower frequencies with decreasing temperature indicating an increase in the refractive index. Moreover, the transmission significantly drops above 1.3 THz at 300 K and above 1.1 THz at 5 K, indicating the presence of an absorption line. This absorption line is absent in pure $Gd_3Fe_5O_{12}$ [30], which suggests that this could be a phonon mode involving Bi in the interstitial sites. This notion is reinforced by the appearance of a Raman-active optical phonon at 1.8 THz when substituting Gd with Tb in $Gd_{2.34}Tb_{0.66}Fe_5O_{12}$ [31]. Without changing the coupling strength, the mass ratio between the Tb and Bi ions would lower this phonon frequency to ≈1.6 THz. Furthermore, room temperature Raman measurements (Fig. 5) show the presence of a peak at 1.28 THz. According to the mutual exclusion principle [32], the appearance of this mode in both Raman and IR spectra can be explained by the lowering of the crystal symmetry due to the random distribution of Bi dopants in GdBIG [33].

Next, TPOP spectroscopy was performed. Figure 2(a) shows THz-induced polarization rotation at three distinct temperatures of 130 K, 100 K, and 80 K. The time traces indicate a rich dynamics which is strongly temperature dependent. The corresponding spectra are plotted in Fig. 2(b) showing multiple peaks. Two of the most pronounced features, centered at 0.135 THz and 0.27 THz, do not move with temperature, while the frequency of the 0.4 THz peak at 130 K increases to 0.7 THz upon lowering the temperature down to 80 K. The extracted peak position with a temperature step of 2 K is shown in Fig. 3(a), in an excellent agreement with the temperature dependence observed for the exchange resonance between the Gd and Fe sublattices [34]. The positions of the other visible peaks in Fig. 2(b) that do not change with temperature within measurement accuracy are consistent with the 1st and the 2nd cavity modes in Fig. 1(b). Therefore, they can convincingly be attributed to the forced response of the spin system to the THz pulse, shaped by multiple reflections at GdBIG surfaces. Moreover, the cavity modes modify the observable linewidth of the magnetic resonance, thereby enabling control of the apparent effective damping of the exchange mode, α_{exch}^{eff}. The apparent change in damping results from the recurrent parametric excitation of the spin system by a phase-matched sequence of the THz pulses within the cavity. The extracted linewidth of the exchange mode at every temperature is shown in Fig. 3(b). The value of α_{exch}^{eff} varies from 0.007 to 0.04 in the observed temperature range. This is almost one order

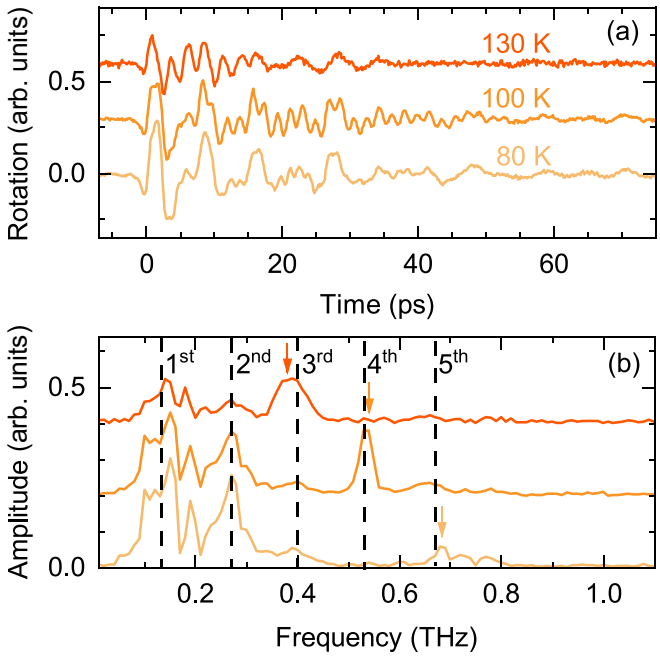

FIG. 2. Temperature dependence of the Gd-Fe exchange mode. (a) THz-induced polarization rotation for 80 K, 100 K, and 130 K, offset for better visibility. (b) FT spectra of the time traces from panel (a); the arrows indicate the exchange mode, offset for better visibility. The vertical dashed lines correspond to the positions of cavity modes calculated under the assumption of a constant terahertz refractive index $n = 5.6$.

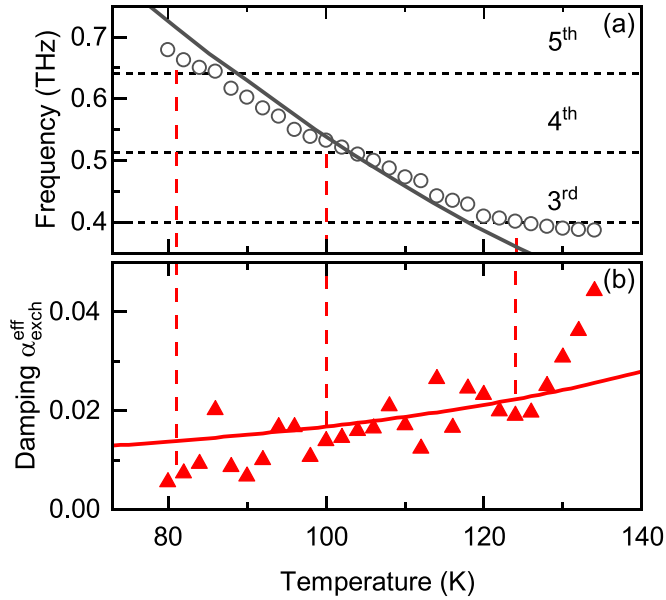

FIG. 3. Exchange mode line analysis. (a) The frequency and (b) the effective damping of the exchange mode as a function of temperature. Both values are extracted with a Lorentzian function fit; see Fig. 10. The black line shows a fit based on the Kaplan-Kittel exchange resonance formula (see Eq. (A5) and Ref. [18]) with the molecular field parameter $N_{\text{Gd-Fe}} = -0.80\ \frac{\text{mol}}{\text{cm}^3}$. The horizontal dashed lines correspond to the positions of cavity modes. The red line is a fit with $\alpha^{\text{eff}}_{\text{exch}} = \alpha^{\text{eff}}(|\vec{M}_{\text{Gd}}| + |\vec{M}_{\text{Fe}}|)/(|\vec{M}_{\text{Gd}}| - |\vec{M}_{\text{Fe}}|)$ [35] with the constant effective Gilbert damping factor of the sublattices $\alpha^{\text{eff}} = 0.0046$.

of magnitude lower than previously reported measurements on similar compounds. With a nonresonant excitation, the intrinsic damping of the exchange mode was shown to be from 0.05 to 0.1 [36]. Rigorous estimation of the enhancement is challenging due to limitations in frequency resolution and the low finesse of the cavity. However, we observed that the enhancement is consistent with the finesse, measuring 5–6 in our experiment.

Note that in the case of optomagnetic excitation of the exchange mode [11], much weaker recurrent magnon pumping can be anticipated. Indeed, owing to the smaller GdBIG refractive index in the visible range [37], subsequent reflected optical pulses will be strongly attenuated. This is in contrast with the Zeeman torque-like excitation by the THz magnetic field, where the larger refractive index results in a high reflectance at the interfaces. Additionally, the optomagnetic mechanism relies on the square of the optical field. Thus, the excitation efficiency decays rapidly for the reflected pulses. In contrast, linear (Zeeman) excitation of the spin exchange mode by THz magnetic field ensures a relatively high efficiency or, in other words, an elevated finesse of the crystal cavity. These two considerations illustrate the excellent suitability of THz radiation for the cavity-enhanced optomagnetic interactions in ferrimagnetic dielectrics.

Controlling the exchange mode necessitates understanding the underlying excitation mechanism. To this end, the THz field strength dependence of the induced magnetization dynamics was analyzed. As illustrated in Fig. 4(a), the amplitude scales linearly with the strength of the THz field. Moreover, the variations of exchange mode amplitude with changing THz field polarization $\beta = \angle(\vec{M}, \vec{H}_{\text{THz}})$, with the net magnetization $\vec{M} = \vec{M}_{\text{Fe}} + \vec{M}_{\text{Gd}}$ and the magnetic field of the THz pump $\vec{H}_{\text{THz}}$, shown in Fig. 4(b), reveals a sinelike dependence. The two observed maxima at $\beta = 90°$ and $\beta = -90°$ are in agreement with the linear Zeeman torque excitation mechanism [25].

Taking advantage of the high tunability of the exchange mode with temperature, we analyzed its coupling with the cavity modes and their influence on the resulting spin dynamics. Figure 4(c) shows the amplitude of the exchange mode as a function of its frequency, where each data point corresponds to a distinct temperature. Although the net magnetic moment of GdBIG significantly decreases as the temperature approaches the compensation point $T_{\text{comp}} = 223$ K [10], this monotonic trend does not account for the observed periodic behavior. However, consistently with the Zeeman torque excitation mechanism, the amplitude of the exchange mode linearly depends on the THz field strength. To illustrate this, we present the FT spectrum of the magnetic field component of the transmitted THz pulse, $H_{\text{THz}} \propto E_{\text{Sam}}$, measured with EOS at 100 K, shown as a gray background in Fig. 4(c). Indeed, the exchange mode amplitude increases twofold when its frequency matches one of the cavity resonances.

Although the coupling results in a noticeable amplification of the exchange mode at the temperatures where its frequency

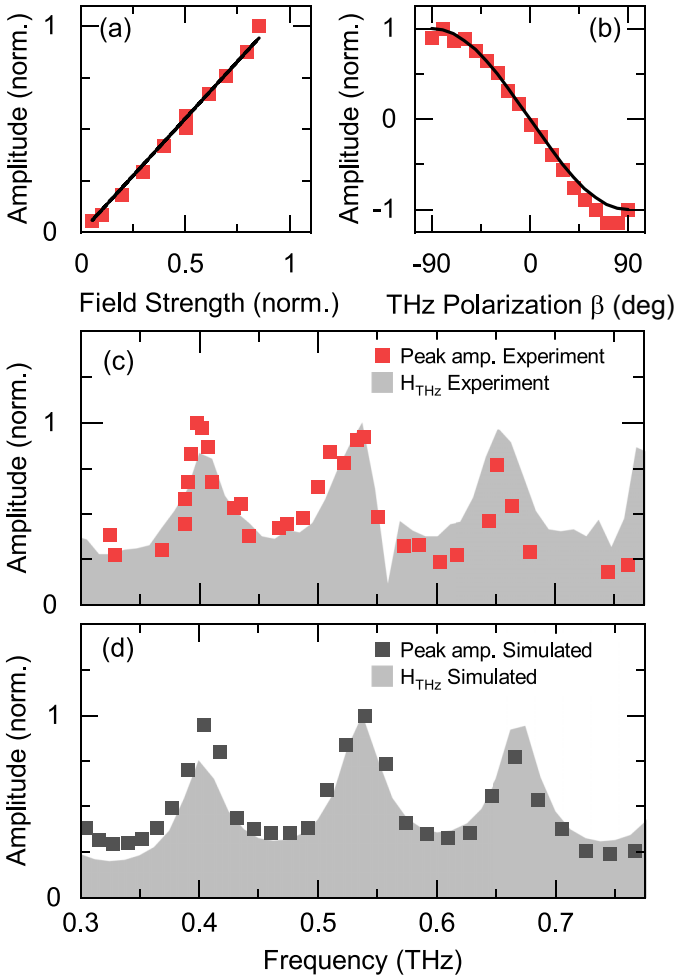

FIG. 4. THz light–exchange mode coupling mechanism. The exchange mode amplitude as a function of (a) THz pulse field strength and (b) THz field polarization. These measurements were performed at a temperature of 100 K. The solid lines are the expected dependencies for a Zeeman excitation mechanism. (c) Amplitude of the exchange mode as function of its frequency, extracted using the same Lorentzian fit applied in Fig. 3. The spectrum of the transmitted pulse train corresponding to the magnetic field of the THz pulse H_{THz} is shown as a gray background. (d) Amplitude of the exchange mode as function of its frequency derived from the simulations (see Sec. IV). The simulated excitation spectrum of H_{THz} is shown as a gray background. The amplitude of the exchange mode was extracted at the frequency calculated using Eq. (A5).

matches those of one of the cavity modes [see Fig. 4(c)], no avoided crossing of the mode dispersion is observed [see Fig. 3(a)], indicating the weak-coupling regime. Estimations show that high loss of the crystal cavity is the main limiting factor which precludes reaching the strong-coupling regime. A promising direction of cavity engineering thus consists of improving the reflectance of the THz radiation at interfaces (see Appendix) for efficient coupling of light with magnetization.

IV. THEORETICAL ANALYSIS AND DISCUSSION

To understand the THz-induced magnetization dynamics in the presence of cavity modes, we employ the modified Landau–Lifshitz–Gilbert equation formalism. Taking into account the dominant role of the iron-iron exchange, the magnetization dynamics can be described by coupled equations for a two-sublattice ferrimagnet [38]:

$$\frac{d\vec{M}_{\mathrm{i}}}{dt} = -(\mu_0\gamma_{\mathrm{i}})\left[\vec{M}_{\mathrm{i}} \times \vec{H}_{\mathrm{i}}^{\mathrm{eff}}\right] - (\mu_0\gamma_{\mathrm{i}})\frac{\alpha_{\mathrm{i}}}{|\vec{M}_{\mathrm{i}}|}\vec{M}_{\mathrm{i}} \times \left[\vec{M}_{\mathrm{i}} \times \vec{H}_{\mathrm{i}}^{\mathrm{eff}}\right] \tag{1}$$

with μ_0 the vacuum magnetic permeability, M_{i} the net magnetizations, γ_{i} the gyromagnetic ratios, and α_{i} the Gilbert damping factors of the Gd and Fe sublattice dynamics. $\vec{H}_{\mathrm{i}}^{\mathrm{eff}}$ is the effective magnetic field defined as

$$\vec{H}_{\mathrm{Gd,Fe}}^{\mathrm{eff}} = \vec{H}_{\mathrm{app}} + \vec{H}_{\mathrm{THz}} - N_{\mathrm{Gd\text{-}Fe}}\vec{M}_{\mathrm{Fe,Gd}}. \tag{2}$$

Here, the first term with $\mu_0\vec{H}_{\mathrm{app}} = 150$ mT represents the external dc magnetic field, $\vec{H}_{\mathrm{THz}}$ denotes the THz pulse magnetic field, and $N_{\mathrm{Gd\text{-}Fe}}$ the effective Gd-Fe exchange parameter. To model the impact of the cavity, we introduce multiple delayed THz pulses so that the temporal profile of the THz stimulus closely follows the experimentally observed transmitted field E_{Sam} in Fig. 1(b) at 80 K. A comparison of the simulated and measured THz wave forms and FT spectra is presented in Figs. 6(a) and 6(b) of Appendix 2.

The exchange field responsible for the coupling of the Gd and joint Fe sublattices is represented by the last term in Eq. (2). It is worth noting that the two-sublattice model can be obtained as a limiting case of the full three-sublattice description, where the Fe-Fe exchange interaction is infinitely stronger than the Gd-Fe one. This three-sublattice formalism is bulky yet instructive, relating an effective $N_{\mathrm{Gd\text{-}Fe}}$ parameter to the parent molecular field coefficients N_{cd} and N_{ca}. Moreover, it is capable of accounting for the temperature dependence of the effective Gd-Fe coupling, which can be highly relevant in our case. Our analysis (see Appendix 3), however, indicates very small ($\sim$1%) variations of $N_{\mathrm{Gd\text{-}Fe}}$ in the considered temperature range. With that in mind, we retain the two-sublattice approach to fit the exchange mode frequency with the Kaplan-Kittel resonance [see Fig. 3(a)]. We obtain $N_{\mathrm{Gd\text{-}Fe}} = -0.8\ \frac{\mathrm{mol}}{\mathrm{cm}^3}$, in good agreement with the value derived from the three-sublattice model (see Appendix 3). Far away from the compensation point $T_{\mathrm{comp}} = 223$ K, it is safe to assume that the Gilbert damping factors are equal $\alpha_{\mathrm{Fe}} = \alpha_{\mathrm{Gd}} = \alpha$ [35] and almost temperature independent [36], while their values were set to 0.03 based on the previous measurements on this very sample [10]. The gyromagnetic ratios are assumed equal as well $\gamma_{\mathrm{Fe}} \approx \gamma_{\mathrm{Gd}} = \gamma = 28\ \frac{\mathrm{GHz}}{\mathrm{T}}$ [38].

By numerically solving Eq. (1) using the Euler method, the magnetization dynamics of the sublattices was extracted. To compare the simulation results with the experiment it is important to note that the Faraday rotation at 800 nm, in our experimental geometry, is mostly sensitive to the magnetization of the iron sublattice in GdBIG [10]. Figure 6(c) shows the simulated and experimentally observed THz-induced magnetization dynamics at 80 K. All corresponding spectra plotted in Fig. 6(d) indicate the presence of the exchange mode. The dispersion of the refractive index of GdBIG was found to have a negligible effect on magnetization dynamics in the studied frequency range. However, as noted from the experiment, the dynamics are strongly dominated by

the low-frequency 1st and 2nd cavity modes. To reproduce this feature, we account for the phase-matching effects between the THz pulse and the optical probe, analogously to [39]. Indeed, significantly better agreement with the experimental results is observed. At the same time, aiming specifically to reproduce the exchange mode temperature behavior rather than the full transient response, we employed the simplest approach, assuming a constant effective THz refractive index n. Simulating temperature changes by varying the sublattice magnetizations allows us to extract the amplitude and the frequency of the exchange mode shown in Fig. 4(d). The gray background illustrates the spectrum of the applied THz magnetic field H_{THz}. Similarly to the experiment, the amplitude of the exchange mode is enhanced when its frequency coincides with the cavity modes created by the sample interfaces.

We believe that the concept of driving high-frequency spin dynamics with a THz pulse train in a cavity formed by the crystal interfaces can be further explored. For example, we suggest a sandwich structure consisting of a THz generation crystal and a ferrimagnet capped by optically transparent and highly THz reflective interfaces. The progress in THz coating makes it possible to achieve very high reflection coefficients, which accentuate the action of the THz pulse train on the medium. For example, indium-tin-oxide-coated glass has THz amplitude reflection coefficient r as high as 0.9 [40], while using THz Bragg mirrors this value potentially can reach 0.99 [41]. This is substantially higher than that obtained in a bare GdBIG crystal with Fresnel reflection at interfaces, where we estimate $r = 0.7$. To study the impact of interface reflection, we simulate THz-induced magnetization dynamics with $r = 0.95$ and plot the amplitude as a function of the frequency of the exchange mode in Fig. 7(a). A much higher dynamical range of the mode amplitude variations is observed, while $\alpha_{\mathrm{exch}}^{\mathrm{eff}}$ can be further reduced by fourfold. This is illustrated in Fig. 7(b) by comparing magnetization dynamics wave forms at a temperature of 128 K. Moreover, in conjunction with using ferrimagnets with much lower intrinsic damping, e.g., yttrium iron garnet [42], exchange mode coupling with THz light might even enter the strongly coupled regime [43,44].

V. CONCLUSION

In conclusion, we investigated the coupling between light at THz frequencies and the Gd-Fe spin exchange mode in GdBIG using THz-pump optical-probe measurements. We show that tuning the exchange mode into a resonance with the cavity modes strongly enhances the efficiency of the THz excitation of high-frequency spin dynamics. The excitation mechanism is attributed to the Zeeman torque. Moreover, the cavity reduces the effective damping of the exchange mode fivefold. The results are analyzed by means of numerical simulations based on a system of coupled Landau–Lifshitz–Gilbert equations which show a good agreement with the experimental observations. A three-subsystem approach developed here allowed us to conclude that the effective Gd-Fe molecular field strength exhibits no variations in the 70–130 K temperature range. This work improves the understanding of efficient control of the exchange modes at THz frequencies.

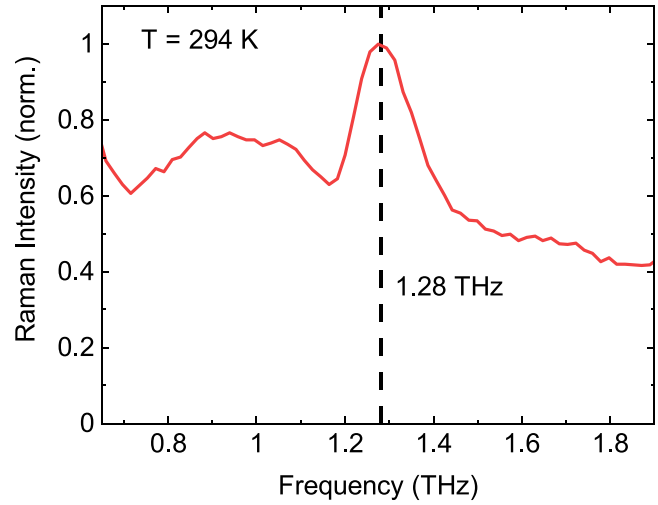

FIG. 5. Raman intensity measured on GdBIG in parallel polarization configuration at room temperature.

Furthermore, it opens an intuitively clear and uncomplicated path to achieve strong coupling between light and sub-THz exchange modes by designing the effective interfaces of a magnetic material.

ACKNOWLEDGMENTS

We thank T. Satoh for providing the samples and fruitful discussions. This work was supported by the DFG, Project No. 277146847–Collaborative research Center 1238: Control and Dynamics of Quantum Materials (Subproject No. B05) and by the project co-financed by the European Union and the Ministry of Education, Youth and Sports of the Czech Republic, TERAFIT-CZ.02.01.01/00/22_008/0004594. C.K. and F.K. acknowledge the support of the Czech Science Foundation, Project No. 25-16097S.

DATA AVAILABILITY

The data that support the findings of this article are openly available [45].

APPENDIX

1. Raman measurement

The Raman spectrum was recorded by a triple-grating spectrometer using a 532 nm continuous wave laser in backscattering geometry at a power of 1 mW on the sample. The direction of polarization of the analyzed light was parallel to that of the incoming beam. The Raman spectrum in the relevant spectral range is shown in Fig. 5.

2. Modeling of THz magnetic field

To model the THz pulse magnetic field H_{THz}, we used sequences of pulses defined as

$$H_{\mathrm{THz}}(t) = H_0 \sum_{k=0}^{N} r^{2k} \cdot \sin(\omega_0 t - k \cdot \omega_0 \tau) \cdot e^{-(t-k\cdot\tau)^2/2\sigma^2}, \tag{A1}$$

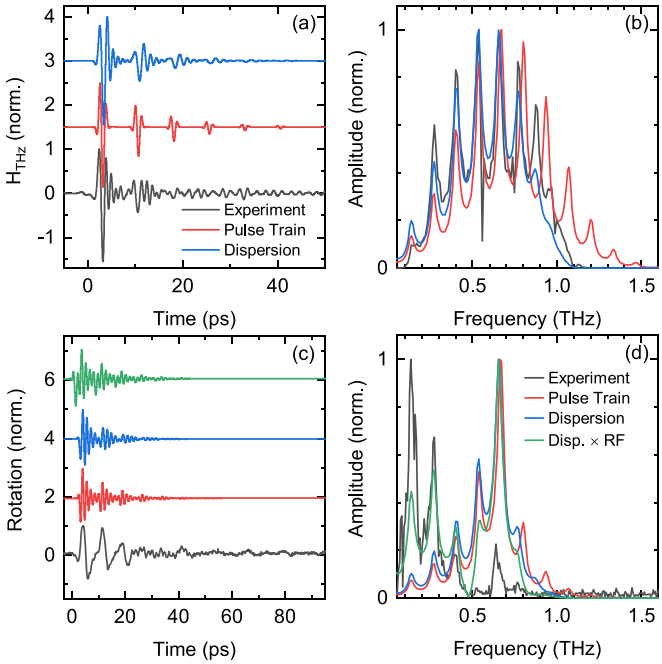

FIG. 6. (a) Magnetic THz field applied in the simulation: a pulse train created by multiple reflections at crystal interfaces, accounting for the dispersion of the complex refractive index at THz frequencies (blue curve) and assuming a constant THz refractive index of $n = 5.6$ and no absorption (red curve). The experimentally measured THz field transmitted through the sample at 80 K (gray curve). (b) Corresponding FT spectra. (c) Resulting transient magnetization response to the magnetic THz field in panel (a): a pulse train with (blue curve) and without (red curve) dispersion effects, as well as with phase-matching detection accounted for (green curve). The latter is achieved by multiplying the result of simulation by the response function (RF), analogously to [39]. The experimentally measured THz-induced magnetization at 80 K (gray curve). (d) Corresponding FT spectra.

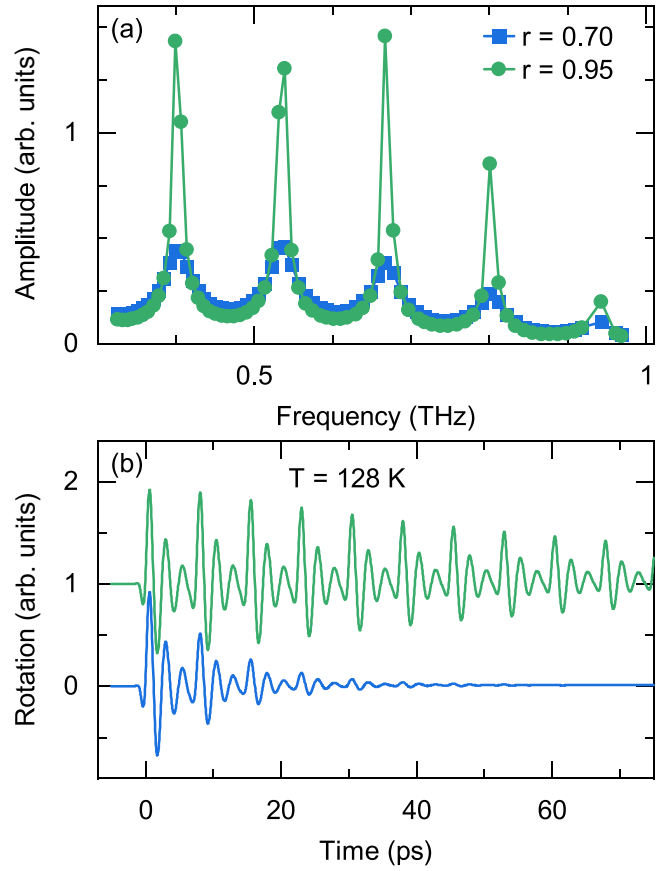

FIG. 7. (a) Numerical simulation of the behavior of the exchange mode amplitude as a function of its frequency with two different reflection coefficients at the interface. (b) THz-induced magnetization dynamics modeled with the reflection coefficient $r = 0.7$ (bottom curve) and $r = 0.95$ (top curve).

with H_0 the magnetic field amplitude, ω_0 the center frequency, σ the pulse duration, N the number of reflections, r the amplitude reflection coefficient at the crystal interface, and τ the time delay introduced by propagation in the medium. To follow the shape of the THz pulse used in the experiment we choose $\mu_0 H_0 = 0.266$ T, $\omega_0/2\pi = 0.6$ THz, and $\sigma = 0.63$ ps. The coefficients $r = (n-1)/(n+1)$ and $\tau = 2nL/c_0$ are calculated using a constant refractive index of $n = 5.6$ extracted from the THz-TDS measurements in Fig. 1, where c_0 is the speed of light in vacuum and the crystal thickness $L = 200$ μm. $N = 10$ is selected to ensure that all reflections within the chosen time window are accounted for. Figure 6(a) shows the resulting sequences of THz pulses compared to the THz electric field measured with EOS after transmitting through the sample at 80 K. A very good agreement of the corresponding spectra is also evident; see Fig. 6(b). To compare the THz-induced magnetization dynamics with that observed in the experiment we plot the out-of-plane component of $\vec{M}_{\mathrm{Fe}}$ in Fig. 6(c) and corresponding spectra in Fig. 6(d).

This approach allows for the testing of different paths to optimize the excitation efficiency of the exchange mode. Figure 7 shows the simulation results of THz-induced spin dynamics with the reflection coefficients at the interfaces of $r = 0.95$. The other parameters are kept the same. It is seen that improving the cavity finesse up to 60 results in a threefold enhancement of the dynamic range of the spin exchange mode peak amplitude (green circles).

3. Effective exchange constant

Rare earth iron garnets are typically considered two-sublattice magnets. This assumption is based on the fact that the molecular field coefficient N_{ad}, which accounts for the interaction between iron at the octahedral and tetrahedral sites, is much larger than the iron–rare earth (rare earth is indexed by c) molecular field coefficients N_{cd} and N_{ca} [46]. For that reason, the majority of recent papers do not address the connection between the effective coupling constant $N_{\mathrm{Gd\text{-}Fe}}$ and the three-sublattice molecular field coefficients. However, this assumption potentially overlooks the temperature dependence of the effective coupling constant [47]. Considering a three-sublattice model instead provides an additional way to estimate $N_{\mathrm{Gd\text{-}Fe}}$ by analyzing SQUID data in combination with molecular field theory. The main steps for deriving $N_{\mathrm{Gd\text{-}Fe}}$ are provided below.

To address the dynamics of a three-sublattice magnet, we write three Landau–Lifshitz equations assuming no damping for simplicity:

$$\frac{d\vec{M}_\mathrm{a}}{dt} = -(\mu_0\gamma_\mathrm{Fe})[\vec{M}_\mathrm{a} \times (\vec{H}_\mathrm{THz} - N_\mathrm{ad}\vec{M}_\mathrm{d} - N_\mathrm{ac}\vec{M}_\mathrm{c})],$$
$$\frac{d\vec{M}_\mathrm{d}}{dt} = -(\mu_0\gamma_\mathrm{Fe})[\vec{M}_\mathrm{d} \times (\vec{H}_\mathrm{THz} - N_\mathrm{da}\vec{M}_\mathrm{a} - N_\mathrm{dc}\vec{M}_\mathrm{c})],$$
$$\frac{d\vec{M}_\mathrm{c}}{dt} = -(\mu_0\gamma_\mathrm{Gd})[\vec{M}_\mathrm{c} \times (\vec{H}_\mathrm{THz} - N_\mathrm{ca}\vec{M}_\mathrm{a} - N_\mathrm{cd}\vec{M}_\mathrm{d})]. \quad \text{(A2)}$$

Then, we look for a solution in the form $\vec{M}_i = \vec{M}_i^{\mathrm{init}} + \vec{m}_i e^{i2\pi ft}$, where $\vec{M}_i^{\mathrm{init}}$ are the ground state magnetizations, $\vec{m}_i$ are the corresponding perturbations, and i corresponds to the indices a, d, and c. We assume that all magnetizations are collinearly aligned in the ground state; note that $N_\mathrm{ad} = N_\mathrm{da}$, $N_\mathrm{ca} = N_\mathrm{ac}$, and $N_\mathrm{cd} = N_\mathrm{dc}$; take into account terms only linear on $\vec{m}_i$ and exclude terms of the second order on N_ac and N_dc. Then, the Gd-Fe exchange frequency $f_\mathrm{Gd\text{-}Fe}$ can be found:

$$f_\mathrm{Gd\text{-}Fe} = \frac{\mu_0\gamma}{2}[N_\mathrm{ad}(M_d - M_a) - N_\mathrm{ac}(M_a + M_c) + N_\mathrm{dc}(M_d - M_c)] - \frac{\mu_0\gamma}{2}\big[N_\mathrm{ad}^2\big(M_a^2 + M_d^2 - 2M_aM_d\big) - 2N_\mathrm{ac}N_\mathrm{ad}\big(M_a^2 + M_aM_c - M_aM_d + M_cM_d\big) - 2N_\mathrm{ad}N_\mathrm{dc}\big(M_d^2 - M_aM_d - M_aM_c - M_cM_d\big)\big]^{1/2}, \quad \text{(A3)}$$

$$f_\mathrm{Gd\text{-}Fe} = \frac{\mu_0\gamma}{2}[N_\mathrm{ad}(M_d - M_a) - N_\mathrm{ac}(M_a + M_c) + N_\mathrm{dc}(M_d - M_c)] - \frac{\mu_0\gamma}{2}N_\mathrm{ad}(M_d - M_a) \times \left[1 - 2\left(\frac{N_\mathrm{ac}}{N_\mathrm{ad}}\right)\frac{M_a^2 + M_aM_c - M_aM_d + M_cM_d}{M_a^2 + M_d^2 - 2M_aM_d} - 2\left(\frac{N_\mathrm{dc}}{N_\mathrm{ad}}\right)\frac{M_d^2 - M_aM_d - M_aM_c - M_cM_d}{M_a^2 + M_d^2 - 2M_aM_d}\right]^{1/2}. \quad \text{(A4)}$$

Given that the iron-iron exchange interaction considerably exceeds the rare earth–iron exchange interaction, $N_\mathrm{ac}, N_\mathrm{dc} \ll N_\mathrm{ad}$, the last two terms inside the square root in Eq. (A4) represent a small parameter to which a Taylor expansion can be applied. This results in

$$f_\mathrm{Gd\text{-}Fe} \approx -(\mu_0\gamma)N_\mathrm{Gd\text{-}Fe}|M_\mathrm{d} - M_\mathrm{a} - M_\mathrm{c}|; \quad \text{(A5)}$$

$$N_\mathrm{Gd\text{-}Fe} = -\frac{N_\mathrm{cd}M_\mathrm{d} + N_\mathrm{ca}M_\mathrm{a}}{M_\mathrm{d} - M_\mathrm{a}}. \quad \text{(A6)}$$

Equation (A6) clearly shows that since the magnetizations $\vec{M}_\mathrm{d}$ and $\vec{M}_\mathrm{a}$ are temperature dependent, the effective Gd-Fe exchange coupling also exhibits temperature dependence when the three-sublattice model is considered. Substituting molecular field coefficients $N_\mathrm{cd} = 6\ \frac{\mathrm{mol}}{\mathrm{cm}^3}$ and $N_\mathrm{ca} = -3.44\ \frac{\mathrm{mol}}{\mathrm{cm}^3}$ from [46] and deriving M_d, M_a, and M_c from SQUID data [48] give an estimation of $N_\mathrm{Gd\text{-}Fe}$ changing in the range from -0.89 to $-0.90\ \frac{\mathrm{mol}}{\mathrm{cm}^3}$ in the studied temperature range from 80 to 130 K, respectively.

4. Complex terahertz refractive index: Measurement and analysis

To measure the terahertz refractive index with high accuracy a high repetition rate THz-TDS setup was used [49]. The real part n and imaginary part k of the extracted refractive index are shown in Fig. 8. These spectral shapes are expected, given that a phonon is present at 1.28 THz [50]. Moreover, a strong temperature dependence is observed. As the temperature decreases, the point at which k starts to substantially increase shifts to lower frequencies, while n monotonically increases in the entire frequency range, indicating a change in the phonon characteristics. However, since the phonon absorption prevents us from resolving the interval near its oscillation frequency, we are unable to draw any further conclusions on its temperature behavior.

5. Rotation spectra

Figure 9 shows FT spectra of THz-induced polarization rotation at different temperatures, from which the frequency and the effective damping of the exchange mode presented in Fig. 4(c) were extracted. The exchange mode is clearly identified by its strong frequency dependence, while its amplitude shows clear periodic modulation. Moreover, we have noticed that the amplitude of the low-frequency peaks increases with lowering temperature.

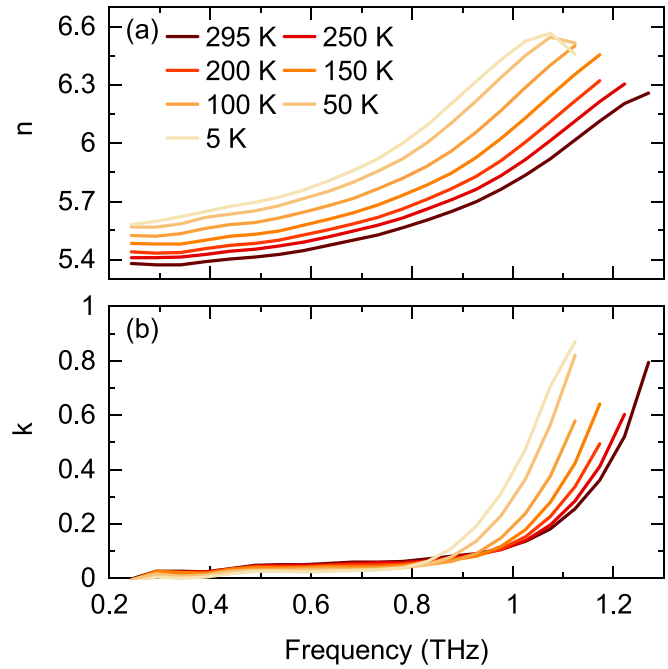

FIG. 8. (a) Real part n and (b) imaginary part k of the refractive index as function of frequency for the specified temperatures.

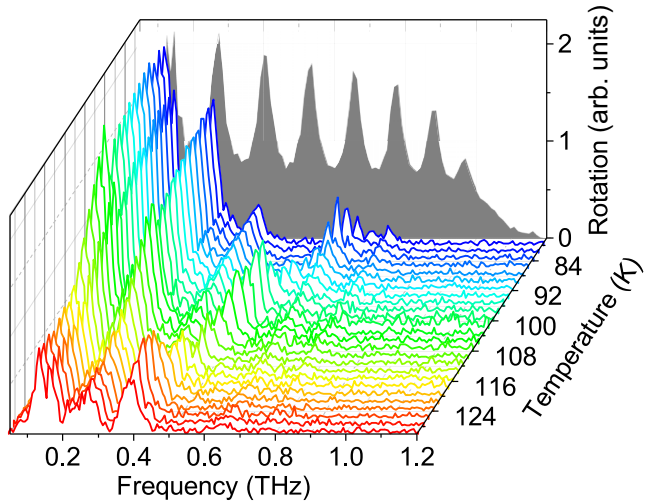

FIG. 9. FT spectra of THz-induced polarization rotation for all temperatures shown in Fig. 4(c). The transmission of the sample in the THz frequency range at 100 K is included as a gray background.

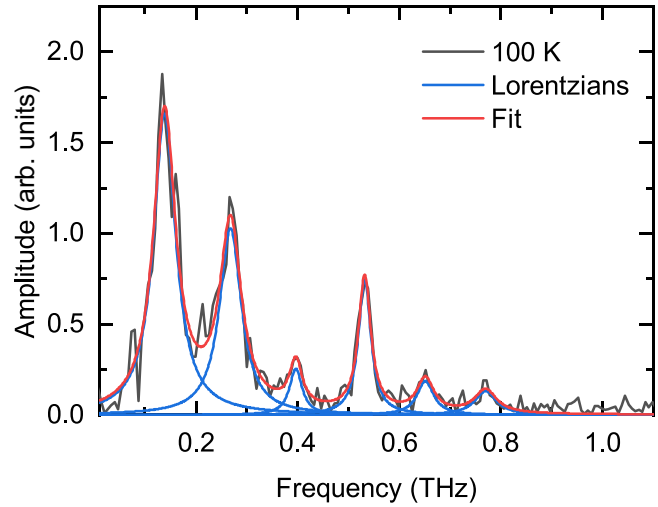

FIG. 10. FT spectrum of THz-induced polarization rotation at 100 K (gray), Lorentzians corresponding to multiple peaks (blue), and the resulting fit (red).

Noting that the polarization rotation of the probe pulse is mainly sensitive to the Faraday effect, we can identify three main factors affecting the amplitudes of the low-frequency peaks: (i) The magneto-optical signal of GdBIG is mostly sensitive to the Fe sublattice magnetic moment, which decreases as the temperature rises; (ii) the magnetic anisotropy continuously increases in this temperature range [48], which slightly changes excitation conditions; (iii) there is a change in the magneto-optical susceptibility of the 800 nm probe pulse. We attribute the latter effect to the presence of the two crystal field transitions (centered at 700 and 900 nm) associated with Fe ions. The above-mentioned factors are expected to result in a smooth, monotonic temperature-dependent behavior and cannot be responsible for the periodic modulation of the exchange mode, which originates in the cavity effects. We have also noticed a kink at 105 K, resulting in a sudden change in amplitude by 15%, which is below the observed modulation of the exchange mode amplitude. The detailed discussion of these factors is beyond the scope of the current paper.

6. Lorentzian fit

To extract the frequency and damping of the exchange mode from the FT spectrum, a number of Lorentzian fit functions were applied. The peak positions closely correspond to the first six cavity modes and the tuneable exchange mode. An example of the fitting procedure at 100 K is shown in Fig. 10.

[1] I. L. Markov, Limits on fundamental limits to computation, Nature (London) **512**, 147 (2014).

[2] P. Wadley, B. Howells, J. Železný, C. Andrews, V. Hills, R. P. Campion, V. Novák, K. Olejník, F. Maccherozzi, S. S. Dhesi, S. Y. Martin, T. Wagner, J. Wunderlich, F. Freimuth, Y. Mokrousov, J. Kuneš, J. S. Chauhan, M. J. Grzybowski, A. W. Rushforth, K. W. Edmonds *et al.*, Electrical switching of an antiferromagnet, Science **351**, 587 (2016).

[3] P. Pirro, V. I. Vasyuchka, A. A. Serga, and B. Hillebrands, Advances in coherent magnonics, Nat. Rev. Mater. **6**, 1114 (2021).

[4] S. Li, L. Zhou, T. Frauenheim, and J. He, Light-controlled ultrafast magnetic state transition in antiferromagnetic-ferromagnetic van der Waals heterostructures, J. Phys. Chem. Lett. **13**, 6223 (2022).

[5] K. Grishunin, E. A. Mashkovich, A. V. Kimel, A. M. Balbashov, and A. K. Zvezdin, Excitation and detection of terahertz coherent spin waves in antiferromagnetic $\alpha-Fe_2O_3$, Phys. Rev. B **104**, 024419 (2021).

[6] H. Qin, R. B. Holländer, L. Flajšman, F. Hermann, R. Dreyer, G. Woltersdorf, and S. van Dijken, Nanoscale magnonic Fabry-Pérot resonator for low-loss spin-wave manipulation, Nat. Commun. **12**, 2293 (2021).

[7] C. Song, Y. You, X. Chen, X. Zhou, Y. Wang, and F. Pan, How to manipulate magnetic states of antiferromagnets, Nanotechnology **29**, 112001 (2018).

[8] K. F. Mak, J. Shan, and D. C. Ralph, Probing and controlling magnetic states in 2D layered magnetic materials, Nat. Rev. Phys. **1**, 646 (2019).

[9] A. Sriram and M. Claassen, Light-induced control of magnetic phases in Kitaev quantum magnets, Phys. Rev. Res. **4**, L032036 (2022).

[10] S. Parchenko, T. Satoh, I. Yoshimine, F. Stobiecki, A. Maziewski, and A. Stupakiewicz, Non-thermal optical excitation of terahertz-spin precession in a magneto-optical insulator, Appl. Phys. Lett. **108**, 032404 (2016).

[11] S. Parchenko, A. Stupakiewicz, I. Yoshimine, T. Satoh, and A. Maziewski, Wide frequencies range of spin excitations in a rare-earth Bi-doped iron garnet with a giant Faraday rotation, Appl. Phys. Lett. **103**, 172402 (2013).

[12] E. A. Mashkovich, K. A. Grishunin, A. K. Zvezdin, T. G. H. Blank, A. G. Zavyalov, P. H. M. van Loosdrecht, A. M.

Kalashnikova, and A. V. Kimel, Terahertz-driven magnetization dynamics of bismuth-substituted yttrium iron-gallium garnet thin film near a compensation point, Phys. Rev. B **106**, 184425 (2022).

[13] T. W. J. Metzger, K. A. Grishunin, C. Reinhoffer, R. M. Dubrovin, A. Arshad, I. Ilyakov, T. V. A. G. de Oliveira, A. Ponomaryov, J.-C. Deinert, S. Kovalev, R. V. Pisarev, M. I. Katsnelson, B. A. Ivanov, P. H. M. van Loosdrecht, A. V. Kimel, and E. A. Mashkovich, Magnon-phonon Fermi resonance in antiferromagnetic CoF_2, Nat. Commun. **15**, 5472 (2024).

[14] W.-H. Hsu, K. Shen, Y. Fujii, A. Koreeda, and T. Satoh, Observation of terahertz magnon of Kaplan-Kittel exchange resonance in yttrium-iron garnet by Raman spectroscopy, Phys. Rev. B **102**, 174432 (2020).

[15] S. Geprägs, A. Kehlberger, F. D. Coletta, Z. Qiu, E.-J. Guo, T. Schulz, C. Mix, S. Meyer, A. Kamra, M. Althammer, H. Huebl, G. Jakob, Y. Ohnuma, H. Adachi, J. Barker, S. Maekawa, G. E. W. Bauer, E. Saitoh, R. Gross, S. T. B. Goennenwein *et al.*, Origin of the spin Seebeck effect in compensated ferrimagnets, Nat. Commun. **7**, 10452 (2016).

[16] E. P. Wohlfarth, *Ferromagnetic Materials*, Vol. 2, 3rd ed. (North-Holland, Amsterdam, 1999).

[17] P. Hansen, P. Röschmann, and W. Tolksdorf, Saturation magnetization of gallium-substituted yttrium iron garnet, J. Appl. Phys. **45**, 2728 (1974).

[18] J. Kaplan and C. Kittel, Exchange frequency electron spin resonance in ferrites, J. Chem. Phys. **21**, 760 (1953).

[19] P. Hansen and J.-P. Krumme, Magnetic and magneto-optical properties of garnet films, Thin Solid Films **114**, 69 (1984).

[20] H. Takeuchi, The Faraday effect of bismuth substituted rare-earth iron garnet, Jpn. J. Appl. Phys. **14**, 1903 (1975).

[21] T. G. H. Blank, K. A. Grishunin, E. A. Mashkovich, M. V. Logunov, A. K. Zvezdin, and A. V. Kimel, THz-scale field-induced spin dynamics in ferrimagnetic iron garnets, Phys. Rev. Lett. **127**, 037203 (2021).

[22] X. Zhang, C.-L. Zou, L. Jiang, and H. X. Tang, Strongly coupled magnons and cavity microwave photons, Phys. Rev. Lett. **113**, 156401 (2014).

[23] G. Jarc, S. Y. Mathengattil, F. Giusti, M. Barnaba, A. Singh, A. Montanaro, F. Glerean, E. M. Rigoni, S. D. Zilio, S. Winnerl, and D. Fausti, Tunable cryogenic terahertz cavity for strong light–matter coupling in complex materials, Rev. Sci. Instrum. **93**, 033102 (2022).

[24] T. G. H. Blank, K. A. Grishunin, and A. V. Kimel, Magneto-optical detection of terahertz cavity magnon-polaritons in antiferromagnetic $HoFeO_3$, Appl. Phys. Lett. **122**, 072402 (2023).

[25] T. Kampfrath, A. Sell, G. Klatt, A. Pashkin, S. Mährlein, T. Dekorsy, M. Wolf, M. Fiebig, A. Leitenstorfer, and R. Huber, Coherent terahertz control of antiferromagnetic spin waves, Nat. Photon. **5**, 31 (2011).

[26] M. Deb, E. Popova, H.-Y. Jaffrès, N. Keller, and M. Bargheer, Controlling high-frequency spin-wave dynamics using double-pulse laser excitation, Phys. Rev. Appl. **18**, 044001 (2022).

[27] H. Hirori, A. Doi, F. Blanchard, and K. Tanaka, Single-cycle terahertz pulses with amplitudes exceeding 1 MV/cm generated by optical rectification in $LiNbO_3$, Appl. Phys. Lett. **98**, 091106 (2011).

[28] Q. Wu and X.-C. Zhang, Free-space electro-optic sampling of terahertz beams, Appl. Phys. Lett. **67**, 3523 (1995).

[29] E. Hecht, *Optics, Global Edition*, 5th ed. (Pearson, London, UK, 2016).

[30] A. J. Sievers and M. Tinkham, Far infrared spectra of rare-earth iron garnets, Phys. Rev. **129**, 1995 (1963).

[31] P. Grunberg, J. A. Koningstein, and L. G. V. Uitert, Optical phonons in iron garnets, J. Opt. Soc. Am. **61**, 1613 (1971).

[32] J. Michael Hollas, *Modern Spectroscopy*, 4th ed. (John Wiley & Sons, Chichester, England, 2003).

[33] P. Kumar, A. I. Maydykovskiy, L. Miguel, N. V. Dubrovina, and O. A. Aktsipetrov, Second harmonic generation study of internally-generated strain in bismuth-substituted iron garnet films, Opt. Express **18**, 1076 (2010).

[34] A. Stupakiewicz and T. Satoh, Ultrafast optomagnonics in ferrimagnetic multi-sublattice garnets, J. Phys. Soc. Jpn. **90**, 081008 (2021).

[35] F. Schlickeiser, U. Atxitia, S. Wienholdt, D. Hinzke, O. Chubykalo-Fesenko, and U. Nowak, Temperature dependence of the frequencies and effective damping parameters of ferrimagnetic resonance, Phys. Rev. B **86**, 214416 (2012).

[36] M. Deb, P. Molho, and B. Barbara, Magnetic damping of ferromagnetic and exchange resonance modes in a ferrimagnetic insulator, Phys. Rev. B **105**, 014432 (2022).

[37] T. Hibiya, O. Okada, and T. Masumoto, Refractive index of Bi-substituted gadolinium iron garnet films grown by liquid-phase epitaxy, J. Appl. Phys. **58**, 510 (1985).

[38] S. Geschwind and L. R. Walker, Exchange resonances in gadolinium iron garnet near the magnetic compensation temperature, J. Appl. Phys. **30**, S163 (1959).

[39] G. Gallot and D. Grischkowsky, Electro-optic detection of terahertz radiation, J. Opt. Soc. Am. B **16**, 1204 (1999).

[40] T. Bauer, J. S. Kolb, T. Löffler, E. Mohler, H. G. Roskos, and U. C. Pernisz, Indium-tin-oxide-coated glass as dichroic mirror for far-infrared electromagnetic radiation, J. Appl. Phys. **92**, 2210 (2002).

[41] Y. Yu, J. Cai, J. Sun, Z. Zhang, and H. Qin, Fabrication and characterization of a wide-bandgap and high-Q terahertz distributed-Bragg-reflector micro cavities, Opt. Commun. **426**, 84 (2018).

[42] V. Cherepanov, I. Kolokolov, and V. L'vov, The saga of YIG: Spectra, thermodynamics, interaction and relaxation of magnons in a complex magnet, Phys. Rep. **229**, 81 (1993).

[43] M. Białek, J. Zhang, H. Yu, and J.-P. Ansermet, Strong coupling of antiferromagnetic resonance with subterahertz cavity fields, Phys. Rev. Appl. **15**, 044018 (2021).

[44] H. Huebl, C. W. Zollitsch, J. Lotze, F. Hocke, M. Greifenstein, A. Marx, R. Gross, and S. T. B. Goennenwein, High cooperativity in coupled microwave resonator ferrimagnetic insulator hybrids, Phys. Rev. Lett. **111**, 127003 (2013).

[45] C. Reinhoffer, I. Razdolski, P. Stein, S. Germanskiy, A. Stupakiewicz, P. H. M. van Loosdrecht, and E. A. Mashkovich, Data and code for "THz Control of Exchange Mode in a Ferrimagnetic Cavity" [Data set], Zenodo (2024), https://doi.org/10.5281/zenodo.12532943.

[46] G. F. Dionne, Molecular field and exchange constants of Gd^{3+}-substituted ferrimagnetic garnets, J. Appl. Phys. **42**, 2142 (1971).

[47] A. E. Clark and E. Callen, Néel ferrimagnets in large magnetic fields, J. Appl. Phys. **39**, 5972 (1968).

[48] S. Parchenko, Laser-induced spin dynamics in multisublattice ferrimagnetic dielectrics, Ph.D. thesis, Repozytorium Uniwersytetu, 2016, http://repozytorium.uwb.edu.pl/jspui/handle/11320/3896.

[49] M. Retuerto, S. Skiadopoulou, F. Borodavka, C. Kadlec, F. Kadlec, J. Prokleška, Z. Deng, J. A. Alonso, M. T. Fernandez-Diaz, F. O. Saouma, J. I. Jang, D. Legut, S. Kamba, and M. Greenblatt, Structural and spectroscopic properties of the polar antiferromagnet Ni_2MnTeO_6, Phys. Rev. B **97**, 144418 (2018).

[50] N. W. Ashcroft and N. D. Mermin, *Solid State Physics* (Holt-Saunders, Orlando, 1976).